

Near-field refrigeration and tunable heat exchange through four-wave mixing

Chinmay Khandekar,^{1, a)} Riccardo Messina,^{2, 1, 3, b)} and Alejandro W. Rodriguez^{1, c)}

¹⁾ *Department of Electrical Engineering, Princeton University, Princeton, NJ 08544, USA*

²⁾ *L2C, Université de Montpellier, CNRS, Montpellier 34095, France*

³⁾ *Laboratoire Charles Fabry, UMR 8501, Institut d'Optique, CNRS, Université Paris-Saclay, Palaiseau Cedex 91127, France*

We modify and extend a recently proposed four-wave mixing scheme [Chinmay Khandekar and Alejandro Rodriguez, *Optics Express*, 25 (19), 23164, 2017] for achieving near-field thermal upconversion and energy transfer, to demonstrate efficient thermal refrigeration at low intensities $\sim 10^9 \text{W/m}^2$ over a wide range of gap sizes (from tens to hundreds of nanometers) and operational temperatures (from tens to hundreds of Kelvins). We further exploit the scheme to achieve magnitude and directional tunability of near-field heat exchange between bodies held at different temperatures.

Near field radiative heat exchange^{1–5} is important for several emerging applications and technologies, from energy conversion^{6,7} to nanoscale heat management and cooling.^{8–11} This has motivated recent efforts aimed at achieving active control of heat transfer using gain media^{12,13} or more generally, chemical potentials.¹⁴ Simultaneous advances in nanofabrication have also made it possible to confine light to small volumes and over long timescales^{15,16}, allowing otherwise weak optical nonlinearities to modify even low-power phenomena like thermal radiation^{17–20}. We recently proposed an alternative mechanism for controlling heat exchange²¹ that exploits nonlinear four-wave mixing to extract and upconvert “thermal energy” trapped in the near field of a planar body unto another, from mid- to near-infrared wavelengths²¹. In particular, we showed that the combination of resonantly enhanced optical nonlinearities and large density of states associated with tightly confined surface plasmon/phonon–polariton (SPP) resonances enables high-efficiency four-wave mixing in planar materials separated by nanoscale gaps, resulting in order 10^5W/m^2 upconversion rates induced by externally incident mid-infrared light of moderate intensities, on the order of 10^{12}W/m^2 .

In this letter, we show that a similar four-wave mixing scheme can be exploited to achieve thermal refrigeration and tunable heat exchange. We begin by exploring the planar configuration shown in Fig. 1(a), comprising an emitter held at temperature T_e and supporting mid-infrared SPP resonances around frequency ω_1 which is separated by a vacuum gap from an absorber held at temperature T_a and supporting near-infrared SPPs around ω_3 . The absorber is coated with a thin $\chi^{(3)}$ nonlinear film supporting a mediator resonance at $\omega_2 \sim (\omega_3 - \omega_1)/2$ which couples to externally incident light by way of a grating. The mediating mode facilitates resonant four-wave mixing ($\omega_1 + 2\omega_2 = \omega_3$) between the SPP resonances, resulting in cooling of the emitter by way of up-

conversion and energy transfer across the gap. As shown below, in contrast to passive radiative cooling mechanisms requiring large temperature differentials $T_e \gg T_a$, nonlinear upconversion allows thermal energy extraction under zero or even negative differentials ($T_e < T_a$), constrained only by photon-number conservation²¹. This in turn enables thermal refrigeration, where thermal energy is made to flow from a low to high temperature body (a reversed heat engine) when the system is driven by external light, which provides the work required for energy transfer. The first part of this letter is devoted to a detailed analysis of such a refrigeration scheme, illustrating not only the various design criteria but also operating regimes needed to achieve high-efficiency refrigeration, including temperature range ($T_e \sim 10\text{--}1000 \text{K}$) and gap sizes. In the second part, we extend the analysis to consider a more complicated system, depicted in Fig. 2(a), where we introduce an additional thin film on top of the nonlinear medium for the purpose of enabling appreciable heat exchange under zero external drive but finite temperature differentials $T_e \neq T_a$, otherwise absent due to the large SPP frequency mismatch between the emitter and absorber. This channel can thus compete with nonlinear energy upconversion to enable tunable heat flow (in both magnitude and direction) with respect to the incident drive power.

A significant refinement in this paper with respect to our earlier work²¹ is the substitution of lossy plasmonic resonances in favor of low-loss dielectric leaky modes in the nonlinear medium. While the latter are less localized than the former, they exhibit longer radiative and absorptive lifetimes and thus result in significantly lower power requirements, on the order of 10^9W/m^2 as opposed to 10^{12}W/m^2 , while also mitigating pump-induced heating. While the choice of transparent materials around the pump wavelength ω_2 mitigates heating introduced by the drive, in practice we expect that efficient thermal cooling will require a vacuum gap (not considered before²¹) in order to further limit conductive transfer stemming from spurious heating. Our theoretical analysis is based on a coupled-mode theory framework,^{22–24} previously exploited to analyze heat transfer in linear media^{25–27} and more recently generalized

^{a)}Electronic mail: cck@princeton.edu

^{b)}Electronic mail: riccardo.messina@umontpellier.fr

^{c)}Electronic mail: arod@princeton.edu

to consider a broad class of weakly nonlinear resonant processes^{28,29}, that provides general operating conditions and quantitative predictions while allowing us to avoid otherwise cumbersome calculations based on nonlinear fluctuational electrodynamics.¹⁷ Finally, we note that our predictions extend recent work in the area of non-contact refrigeration^{12,30,31} and dynamically tunable heat exchange,^{13,32} and has analogies with more established thermoelectric cooling schemes.³³

Thermal refrigeration.—We first consider the planar system shown in Fig. 1(a), comprising a silica (SiO₂) emitter separated by a vacuum gap d from an aluminum-doped zinc oxide (AZO) absorber. The associated dielectric properties are obtained from various references.^{34–36} The nonlinear medium is a chalcogenide (ChG) thin film of material composition As₂S₃, thickness t , permittivity $\epsilon_2 = 6.25$, and isotropic Kerr coefficient $\chi^{(3)} = 10^{-17} \text{ m}^2/\text{V}^2$.^{37–40} (Note that we assume an isotropic Kerr coefficient, $\chi_{xxxx} = 3\chi_{xxyy} = 3\chi_{xyxy} = \chi^{(3)}$, purely for computational and conceptual convenience, but that more generally the nature of the relevant tensor components will depend on growth and material considerations.^{38,41}) The p -polarized SPP resonances in this configuration are characterized by their conserved transverse momenta \mathbf{k} and described by mode profiles of the form $E_l(z)e^{i\mathbf{k}\cdot\mathbf{x}_\parallel}$, where $l \in x, y, z$ and \mathbf{x}_\parallel is the transverse position. Figure 1(b) shows multiple mode dispersions $\omega(k)$ arising in the above configuration, for a choice of $d = 30\text{nm}$, illustrating two branches of SPPs localized at the SiO₂ interface of frequencies $\omega_{1a} \sim 2 \times 10^{14} \text{ rad/s}$ and $\omega_{1b} \sim 0.8 \times 10^{14} \text{ rad/s}$, along with a single SPP branch localized at the AZO interface of frequency $\omega_3 \sim 12 \times 10^{14} \text{ rad/s}$. Also present (not shown) is a separate mediator resonance that propagates primarily within

the ChG film with frequency $\omega_2 \approx 5 \times 10^{14} \text{ rad/s}$ and wavevector $\mathbf{k}_2 = k_2\hat{y}$. This mediator mode can couple to externally incident light at ω_2 and angle θ_{inc} by way of a thin, first-order diffraction grating of period Λ , designed to satisfy $\frac{\omega_2}{c} \sin \theta_{\text{inc}} + \frac{2\pi}{\Lambda} = k_2$. Note that the thin size of the grating ($\lesssim 5\text{nm}$) and large frequency mismatch between the mediator and SPP resonances combine such that the grating has a negligible impact on the dispersions and resonances of the slabs.⁴² Furthermore, four-wave mixing between SPPs is only possible under the momentum-matching condition, $\mathbf{k}_1 + 2\mathbf{k}_2 = \mathbf{k}_3$,²¹ thus ensuring that only a single emitter mode at \mathbf{k}_1 couples exclusively to an absorber mode at \mathbf{k}_3 . In particular, given a set $(\mathbf{k}_1, \mathbf{k}_3)$ of momentum-matched modes, the upconversion rates can be computed using the following coupled mode equations:

$$\begin{aligned} \dot{a}_{1\alpha} &= (i\omega_{1\alpha} - \gamma_{1\alpha})a_{1\alpha} - i\kappa_{1\alpha}e^{-2i\omega_2 t}a_3 - i\kappa_1 a_{1\beta} \\ &\quad + \sqrt{2\gamma_{1\alpha}}\xi_{1\alpha}, \quad \alpha, \beta \in \{a, b\}, \quad \alpha \neq \beta \\ \dot{a}_3 &= (i\omega_3 - \gamma_3)a_3 - \sum_{\alpha=a,b} i\frac{\omega_3}{\omega_{1\alpha}}\kappa_{1\alpha}^*e^{2i\omega_2 t}a_{1\alpha} + \sqrt{2\gamma_3}\xi_3, \end{aligned} \quad (1)$$

where a_j denotes the amplitude of mode $j \in [1a, 1b, 2, 3]$, normalized such that $|a_j|^2$ is the corresponding mode energy and ξ_j represent thermal noise sources with thermodynamic correlations $\langle \xi_j^*(\omega)\xi_j(\omega') \rangle = \Theta(\omega, T_k)\delta(\omega - \omega')$, where $\Theta(\omega, T_j) = \hbar\omega/[\exp(\hbar\omega/k_B T_j) - 1]$ denotes the Planck distribution corresponding to a local bath temperature T_j .⁴³ The mode frequencies $\omega_j(k_j)$ and associated decay rates γ_j are obtained from the complex, eigenfrequency solutions of Maxwell's equations, while the nonlinear coupling coefficients $\kappa_{1\alpha}$ ($\alpha = a, b$) describing four-wave mixing are obtained via perturbation theory^{28,29} and depend on a complicated, spatial overlap of the linear profiles within the nonlinear medium:²¹

$$\kappa_{1\alpha}(\mathbf{k}_1, \mathbf{k}_3) = \frac{\omega_{1\alpha}\gamma_c I \int dz \chi_{ijkl}^{(3)} e^{i(\mathbf{k}_3 - \mathbf{k}_1 - 2\mathbf{k}_2\hat{y})\cdot\mathbf{x}_\parallel} E_{1\alpha,i}(\omega_{1\alpha}, z) E_{2,j}(\omega_2, z) E_{2,k}(\omega_2, z) E_{3,l}^*(\omega_3, z)}{\epsilon_0 \gamma_{2t}^2 (\int dz \frac{\partial \epsilon \omega}{\partial \omega} |E_2(\omega_2, z)|^2) (\int dz \frac{\partial \epsilon \omega}{\partial \omega} |E_{1\alpha}(\omega_{1\alpha}, z)|^2)^{1/2} (\int dz \frac{\partial \epsilon \omega}{\partial \omega} |E_3(\omega_3, z)|^2)^{1/2}}. \quad (2)$$

Here I is the drive intensity and $\gamma_{2t} = \gamma_2 + \gamma_{2c}$ is the overall loss rate of the mediator resonance, which includes both dissipative γ_2 and radiative decay γ_{2c} (induced by the periodic grating). Note that the momentum-matching condition of nonzero coupling follows by inspection of the phase factor $e^{i(\mathbf{k}_3 - \mathbf{k}_1 - 2\mathbf{k}_2\hat{y})\cdot\mathbf{x}_\parallel}$, allowing us to simplify $\kappa_{1\alpha}(\mathbf{k}_1, \mathbf{k}_3) \rightarrow \kappa_{1\alpha}(k, \theta)$, where $k = |\mathbf{k}_1|$ and θ is the angle between \mathbf{k}_1 and the wavevector of the mediator mode (parallel to the y axis). Also included in the coupled-mode equations is the possibility of finite linear coupling κ_l between the two emitter SPPs, which is negligible in the current configuration due to the large discrepancy between ω_{1a} and ω_{1b} but turns out to be of critical importance in the configuration of Fig. 2(b).

From these coupled-mode equations, one can find the various energy transfer rates corresponding to a

given set of modes (k, θ) by considering the overall energy loss rate associated with each mode,²² leading to simple expressions for the thermal extraction $P_{\alpha \rightarrow 3} = 2\langle \text{Im}[\kappa_{1\alpha}^* \exp(2i\omega_2 t) a_3^* a_{1\alpha}] \rangle$ and linear heat transfer $P_{a \rightarrow b} = 2\langle \text{Im}[\kappa_l^* a_{1a} a_{1b}^*] \rangle$ rates, along with associated power spectral densities.²¹ The net flux rates $H_{\alpha \rightarrow \beta}$ are then given by:

$$H_{\alpha \rightarrow \beta} = \int_0^\infty \frac{k dk}{2\pi} \underbrace{\int_0^\infty \frac{d\theta}{2\pi} \int_0^\infty \frac{d\omega}{2\pi} P_{\alpha \rightarrow \beta}(\omega, k, \theta)}_{P_{\alpha \rightarrow \beta}(k, \theta)}, \quad (3)$$

where $\alpha, \beta \in \{a, b, 3\}$ labels the particular flux channel. To provide a proof-of-concept demonstration of thermal refrigeration, we first consider typical geometric and operating parameters, with $d = 30\text{nm}$, $t = 100\text{nm}$, $\Lambda = 2\mu\text{m}$, $\theta_{\text{inc}} = 45^\circ$, and $T_a = 300\text{K}$. Figure 1(c) shows

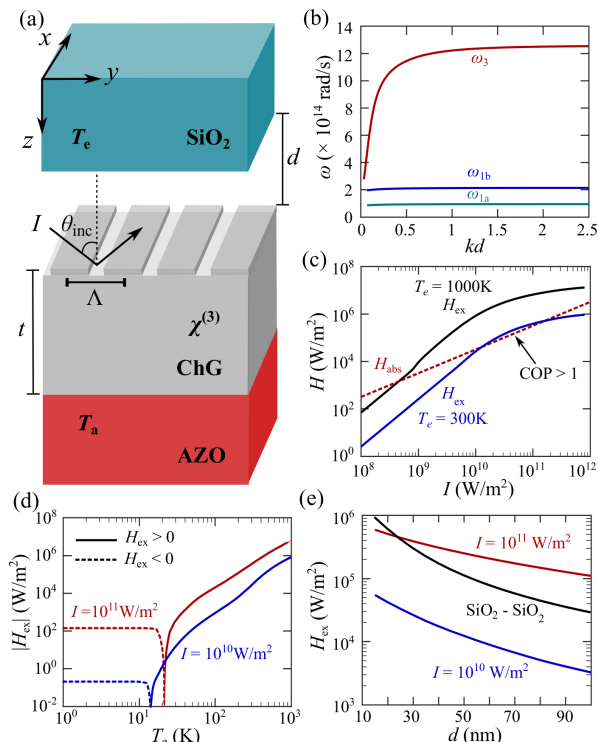


FIG. 1. (a) SiO_2 glass held at temperature T_e is separated by a vacuum gap d from an AZO slab at temperature T_a that is coated with a ChG thin grating of thickness t and period Λ . An external, monochromatic drive of intensity I incident at angle θ_{inc} couples to a leaky mode of frequency ω_2 in the ChG grating that mediates four-wave mixing between SiO_2 ($\sim \omega_{1a}, \omega_{1b}$) and AZO ($\sim \omega_3$) SPPs. For fixed $d = 30$ nm, $t = 100$ nm, $T_a = 300$ K, (b) shows the associated SPP dispersions while (c) shows the extracted power H_{ex} from SiO_2 at two different temperatures T_e (solid), along with the absorbed power H_{abs} in the absorber (dashed), as a function of I . (d) illustrates the dependence of H_{ex} on T_e for two values of drive intensities I , showing a reversal from positive $H_{\text{ex}} > 0$ (solid lines) to negative $H_{\text{ex}} < 0$ (dashed lines) extraction at low temperatures, while (e) shows the dependence on vacuum gap d for the same intensities but fixed $T_e = 300$ K. Also shown for comparison in the same plot is the flux rate between two semi-infinite SiO_2 plates held at temperatures $T_e = 300$ K and $T_a = 0$ K, as a function of d .

the net thermal extraction rate $H_{\text{ex}} = H_{a \rightarrow 3} + H_{b \rightarrow 3}$ corresponding to two different emitter temperatures, $T_e = 300$ K (blue curve) and $T_e = 1000$ K (black curve), as a function of drive intensity I . Evidently, large flux rates $H_{\text{ex}} \sim 10^5$ W/m² are achievable with moderate drive intensities $I \sim 10^9$ W/m², illustrating over three orders of magnitude improvements in power efficiency (reduced intensity requirements) over earlier configurations²¹ based on lossy plasmonic mediator resonances. Note that the transparency of the emitter at pump wavelength as well as the presence of vacuum gap and large SPP frequency mismatch imply that conductive or radiative heating of the emitter due to the pump is negligible compared to heat extraction leading to its cooling. The efficiency of such reversed heat engine (refrigeration scheme) is given by a coefficient of performance³³ (COP), defined as the

ratio of thermal energy extracted to power that is lost to pump-induced heating. It follows from coupled mode equations that the absorbed pump intensity at ω_2 is given by $H_{\text{abs}} = 4\gamma_2\gamma_{2c}I/\gamma_{2t}^2$. We choose the radiative or coupling rate of the mediator mode to be $\gamma_{2c} = 10^{-5}\omega_2$, a very reasonable estimate based on extensive theoretical^{44–46} and experimental work on similar thin gratings.⁴² The dissipation rate $\gamma_2 \approx \text{Im}\{\epsilon_m\}\omega_2/2\text{Re}\{\epsilon_m\}$ where ϵ_m is the complex permittivity of the nonlinear medium, is obtained from perturbation theory and agrees with the exact complex eigenfrequency solution. With $\text{Im}\epsilon_m \approx 10^{-10}$ (obtained from extrapolating available data⁴⁷), it follows that $\gamma_2 \ll \gamma_{2c}$ and as shown by red curve in Fig. 1(c), the absorbed power $H_{\text{abs}} \approx 4\gamma_2I/\gamma_{2c}$ by the ultra-low loss resonance is smaller than the heat extraction rates leading to $\text{COP} \gg 1$ over a varying range of intensities. While such ultra-low loss resonances have been explored extensively in different context⁴⁸, they play an important role here in minimizing the unnecessary power dissipation and enhancing the refrigeration efficiency (COP). While ideally, $\text{COP} > 1$ is within reach, various non-idealities such as fabrication imperfections and spurious material loss rates may lead to effectively larger dissipation rates in actual experiments and potentially smaller values of $\text{COP} \approx 10^{-2}$. We note that these are realistic efficiencies of all such solid-state refrigeration schemes^{31,33} and are acceptable given the reliability (no moving parts) and ease of on-chip implementation in comparison to other gas based refrigeration methods.

Yet another important figure of merit is the range of operating temperatures over which it is possible to cool the emitter (independently of efficiencies). Along this vein, Fig. 1(d) shows H_{ex} as a function of T_e for multiple values of I , illustrating a change in the sign of the flux from positive (solid) to negative (dashed) as T_e decreases past a typical transition temperature $T_e \sim 10$ K. It follows that under ideal conditions under which $T_a = 300$ K is held fixed, heat can be extracted from the emitter until it is cooled down to temperatures on the order of tens of Kelvin. Moreover, while we have chosen so far to focus on configurations involving very small vacuum gaps $d = 30$ nm, as shown in Fig. 1(e), significant flux rates can nevertheless be achieved at larger separations $d \sim 100$ nm. This is an important consideration for current state of the art experiments exploring near-field heat transfer in planar geometries⁵. Interestingly, we find that the complicated dependence of the spectral flux rate on gap and drive intensity, quantified by the coupling coefficient $\kappa(k, \theta)$, leads to a modified relationship between the net flux and gap size compared to the typical $\sim 1/d^2$ dependence associated with linear heat exchange. Comparing H_{ex} in the particular case of $I = 10^{11}$ W/m² and equal $T_e = T_a = 300$ K (solid red line) to the flux rate between two SiO_2 plates held at a large temperature differential, $T_e = 300$ K and $T_a = 0$ K, but separated by the same gap sizes (black line), one finds not only significantly larger extraction rates but also a slower polynomial decay in the former. We fi-

nally remark that apart from the efficiency comparable to other solid-state refrigeration methods^{31,33}, the design flexibility and wide range of temperature regimes achievable through this scheme could prove a viable alternative depending on the application.

Tunable heat exchange: We now consider a slightly modified configuration, depicted schematically in Fig. 2(a), to illustrate the possibility of exploiting four-wave mixing as a means of achieving tunable heat exchange. The modified configuration consists of a silicon carbide (SiC) emitter separated by vacuum from an AZO absorber. Resting on the absorber is a composite layer consisting of an additional SiC thin film of thickness $h = 20\text{nm}$ on top of a nonlinear gallium arsenide (GaAs) film, with nonlinear $\chi^{(3)} = 10^{-18}\text{m}^2/\text{V}^2$ and dielectric properties taken from various references.^{34–36,49} The presence of the additional SiC thin film results in three branches of SPPs, out of which only two, depicted as solid lines in Fig. 2(b), correspond to SPPs localized along the SiC–vacuum interfaces. In contrast to the previous configuration, however, these SPPs have non-negligible linear coupling ($\kappa_l \neq 0$) due to similar resonance frequencies and can therefore contribute significant linear heat exchange between the emitter and absorber. In order to incorporate both nonlinear upconversion and linear heat exchange, we obtain the unperturbed frequencies, mode profiles, and linear coupling rates κ_l of the SPPs by fitting the full linear fluctuational electrodynamics calculations to the coupled-mode equations. The dashed (solid) lines in Fig. 2(b) depict the unperturbed (perturbed) resonance frequencies, $\omega_{1a} \sim \omega_{1b} \sim 1.8 \times 10^{14}\text{rad/s}$, obtained using the fitting procedure. In addition, the system supports a SPP branch around frequency $\omega_3 \sim 10 \times 10^{14}\text{rad/s}$ that is localized along the AZO interface, shown as an inset (red line). Like before, a thin grating of period $\Lambda = 1.78\ \mu\text{m}$ is used to couple incident light at angle $\theta_{\text{inc}} = 45^\circ$ to a mediator resonance in the GaAs film of frequency $\omega_2 \approx 4 \times 10^{14}\text{rad/s}$ and wavevector $\mathbf{k}_2 = k_2\hat{y}$.

To provide a proof-of-concept demonstration of tunable heat exchange, we consider a typical set of parameters, corresponding to $d = 50\text{nm}$, $h = 20\text{nm}$, $t = 100\text{nm}$, and $T_e = 300\text{K} < T_a = 400\text{K}$, which in the absence of the drive nevertheless leads to a net heat exchange across the gap directed toward the emitter. Figure 2(c) shows the net $H_{\text{ex}} = H_{a \rightarrow b} + H_{a \rightarrow 3}$ (black line) along with individual $H_{a \rightarrow b}$ (blue line) and $H_{a \rightarrow 3}$ (red line) extraction rates, as a function of drive intensity I . Evidently, at low drive intensities $I \ll 10^{12}\text{W/m}^2$, the net extraction rate H_{ex} is dominated by the linear heat exchange between the SiC resonances ($H_{a \rightarrow b} < 0$), becoming gradually larger due to nonlinear extraction ($H_{a \rightarrow 3} > 0$) with increasing I , with the reversal in heat flow across the gap occurring at $I \gtrsim 10^{13}\text{W/m}^2$. Note that while intuitively one might expect a decreasing amount of linear heat flow with increasing nonlinear upconversion, we observe a non-monotonic trend in $H_{a \rightarrow b}$ with increasing I that demonstrates instead an increase in linear

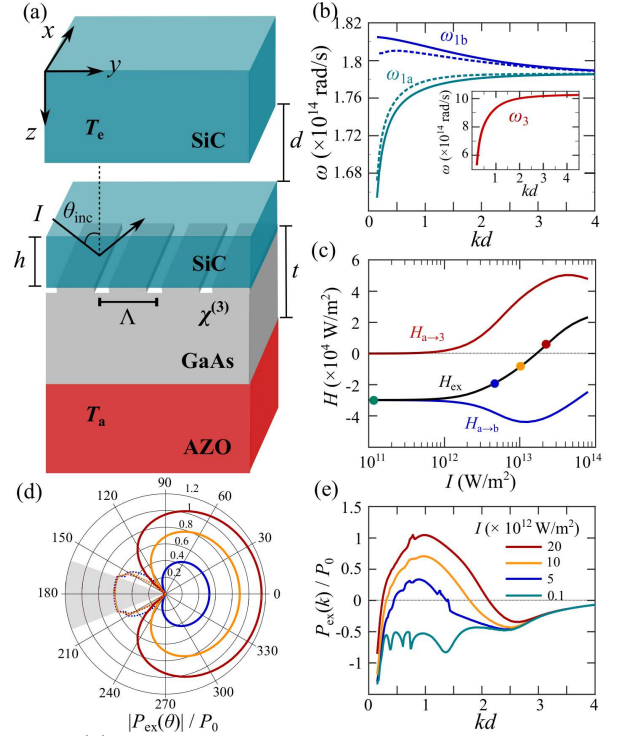


FIG. 2. (a) SiC emitter separated by a $d = 50\text{nm}$ vacuum gap from an AZO absorber that is coated with a composite layer consisting of a SiC film (thickness $h = 20\text{nm}$) on top of a nonlinear GaAs film (thickness $t = 100\text{nm}$). The thin periodic grating couples externally incident light at ω_2 in GaAs, mediating four-wave mixing between various SPP resonances, with dispersions shown in (b), localized to both AZO (ω_3) and SiC (ω_{1a}, ω_{1b}) interfaces, where solid (dashed) lines denoting perturbed (unperturbed) modes (see text). Assuming a temperature differential, $T_e = 300\text{K}$ and $T_a = 400\text{K}$, (c) shows the net extraction power from the SiC slab across the gap H_{ex} , along with the individual nonlinear $H_{a \rightarrow 3}$ and linear $H_{a \rightarrow b}$ contributions, illustrating the possibility of tunable extraction (in both magnitude and direction) with respect to drive intensity I . (d) and (e) illustrate the underlying contribution of individual resonances, classified by their angular and wavevector states, showing the per-angle $P_{\text{ex}}(k, \theta)$ (at $kd = 0.5$) and angle-integrated frequency-integrated flux $P_{\text{ex}}(k)$ (with respect to k), respectively, at multiple I , marked by circles in (c). The flux rates are normalized by $P_0 = 2\gamma_1\Theta(\omega_1, T_e)$, where $\gamma_1 = 4.45 \times 10^{14}\text{rad/s}$ and $\omega_1 = 1.8 \times 10^{14}\text{rad/s}$.

flow at low intensities. Such a non-trivial interplay between the two (linear and nonlinear) processes originates from a shift in the SiC mode frequencies that ends up enhancing the otherwise sub-optimal (due to the slight frequency mismatch) linear heat flow. While the net flux rates contain contributions from a wide set of SPPs, characterized by (k, θ) , the underlying behavior of flux rates for these modes can be analyzed by inspection of the frequency-integrated spectral flux $P_{\text{ex}}(k, \theta)$. For illustration, Fig. 2(d) shows the angular dependence of the flux rate at a fixed $kd = 0.5$, with Fig. 2(e) showing the underlying angle-averaged spectrum with respect to kd at multiple drive intensities, corresponding to the points marked by circles in Fig. 2(c). For convenience, we

normalize these flux rates by $P_0 = 2\gamma_1\Theta(\omega_1, T_e)$, or the thermal power available to a single SPP, for typical values of $\gamma_1 = 4.45 \times 10^{11}$ rad/s and $\omega_1 = 1.78 \times 10^{14}$ rad/s. As illustrated in Fig. 2(d), both the magnitude and direction of the flux rate depend on the angle θ and intensity I , with the latter eventually resulting in large, positive angle-averaged flux rates at larger I . Note that there exists a range of modes, corresponding to highly acute angles (grey region), for which the momentum-matching condition $\mathbf{k}_3 = \mathbf{k}_1 + 2\mathbf{k}_2$ can never be satisfied and for which there is no nonlinear upconversion. Finally, Fig. 2(e) shows the growing contribution and role of modes satisfying momentum-matching in the net exchange, allowing nonlinear upconversion to overwhelm the linear heat flow with increasing I .

Concluding remarks.—We demonstrated a four-wave mixing scheme for active near-field heat extraction. This approach not only enables efficient nanoscale thermal refrigeration at very low temperatures ~ 10 K and low input intensities $I \sim 10^9$ W/m², but also active control of both the magnitude and direction of heat flow across vacuum gaps. While the systems explored in this work represent only a proof of concept, we are confident that other geometries and materials could result in further improvements. We note that the coupled mode approach²¹ employed above is valid as long as the decay and coupling rates are much smaller than the resonant frequencies of SPPs. It breaks down for large intensities $I \gtrsim 10^{14}$ W/m² where not only coupling rates are very large but also other considerations such as optical damage threshold⁵⁰ become important. While coupled mode theory circumvents the need to carry out full and repeated calculations, further analysis of such nanoscale pump-thermal mixing processes using nonlinear fluctuational electrodynamics¹⁷ remains a challenging and interesting problem for future work.

Acknowledgments.— This work was partially supported by the National Science Foundation (DMR-1454836), Princeton Center for Complex Materials with funding from NSF MRSEC program (DMR-1420541) and Cornell Center for Materials Research with funding from the NSF MRSEC program (DMR-1719875).

¹J. J. Loomis and H. J. Maris, Phys. Rev. B **50** (24), 18517 (1994).

²K. Joulain, J.-P. Mulet, F. Marquier, R. Carminati, and J.-J. Greffet, Surf. Sci. Rep. **57** (3), 59 (2005).

³A. I. Volokitin and B. N. J. Persson, Rev. Mod. Phys. **79** (4), 1291 (2007).

⁴S. Basu, Z. M. Zhang, and C. J. Fu, Int. J. Energy Res. **33** (13), 1203 (2009).

⁵B. Song, A. Fiorino, E. Meyhofer, and P. Reddy, Aip Advances **5** (5), 053503 (2015).

⁶A. Narayanaswamy and G. Chen, Appl. Phys. Lett. **82** (20), 3544 (2003).

⁷M. Laroche, R. Carminati, and J.-J. Greffet, J. Appl. Phys. **100** (6), 063704 (2006).

⁸D. G. Cahill, P. V. Braun, G. Chen, D. R. Clarke, S. Fan, K. E. Goodson, P. Keblinski, W. P. King, G. D. Mahan, A. Majumdar et al., Appl. Phys. Rev. **1** (1), 011305 (2014).

⁹D. G. Cahill, W. K. Ford, K. E. Goodson, G. D. Mahan, A. Majumdar, H. J. Maris, R. Merlin, and S. R. Phillpot, J. Appl. Phys. **93** (2), 793 (2003).

¹⁰A. Shakouri, Proceedings of the IEEE **94** (8), 1613 (2006).

¹¹B. Guha, C. Otey, C. B. Poitras, S. Fan, and M. Lipson, Nano Lett. **12** (9), 4546 (2012).

¹²D. Ding, T. Kim, and A. J. Minnich, Phys. Rev. B **93** (8), 081402 (2016).

¹³C. Khandekar, W. Jin, O. D. Miller, A. Pick, and A. W. Rodriguez, Phys. Rev. B **94** (11), 115402 (2016).

¹⁴K. Chen, P. Santhanam, S. Sandhu, L. Zhu, and S. Fan, Phys. Rev. B **91** (13), 134301 (2015).

¹⁵M. Soljačić and J. D. Joannopoulos, Nat. Mater. **3** (4), 211 (2004).

¹⁶D. K. Armani, T. J. Kippenberg, S. M. Spillane, and K. J. Vahala, Nature **421** (6926), 925 (2003).

¹⁷H. Soo and M. Krüger, Europhys. Lett. **115** (4), 41002 (2016).

¹⁸H. Soo and M. Krüger, preprint arXiv:1710.04605 (2017).

¹⁹C. Khandekar, A. Pick, S. G. Johnson, and A. W. Rodriguez, Phys. Rev. B **91** (11), 115406 (2015).

²⁰C. Khandekar, Z. Lin, and A. W. Rodriguez, Appl. Phys. Lett. **106** (15), 151109 (2015).

²¹C. Khandekar and A. W. Rodriguez, Opt. Express **25** (19), 23164 (2017).

²²H. A. Haus, *Waves and fields in optoelectronics* (Prentice-Hall, 1984).

²³S. Fan, W. Suh, and J. D. Joannopoulos, JOSA A **20** (3), 569 (2003).

²⁴Z. Ruan and S. Fan, J. Phys. Chem. C **114** (16), 7324 (2009).

²⁵H. Chalabi, E. Hasman, and M. L. Brongersma, Opt. Express **22** (24), 30032 (2014).

²⁶C. Lin, B. Wang, and K. H. Teo, J. Appl. Phys. **121** (18), 183101 (2017).

²⁷H. Iizuka and S. Fan, J. Appl. Phys. **120** (19), 194301 (2016).

²⁸J. D. Joannopoulos, S. G. Johnson, J. N. Winn, and R. D. Meade, *Photonic crystals: molding the flow of light* (Princeton University Press, 2011).

²⁹A. Rodriguez, M. Soljačić, J. D. Joannopoulos, and S. G. Johnson, Optics express **15** (12), 7303 (2007).

³⁰X. Liu and Z. M. Zhang, Nano Energy **26**, 353 (2016).

³¹K. Chen, T. P. Xiao, P. Santhanam, E. Yablonovitch, and S. Fan, Journal of Applied Physics **122** (14), 143104 (2017).

³²K. Ito, K. Nishikawa, A. Miura, H. Toshiyoshi, and H. Iizuka, Nano Lett. **17**, 4347 (2017).

³³S. Riffat and X. Ma, International Journal of Energy Research **28** (9), 753 (2004).

³⁴E. D. Palik, *Handbook of optical constants of solids*, vol. 3 (Academic press, 1998).

³⁵I. Pirozhenko and A. Lambrecht, Phys. Rev. A **77** (1), 013811 (2008).

³⁶J. Kim, G. V. Naik, N. K. Emani, U. Guler, and A. Boltasseva, IEEE J. Sel. Top. Quantum Electron. **19** (3), 4601907 (2013).

³⁷L. G. Aio, A. M. Efimov, and V. F. Kokorina, J. Non-Cryst. Solids **27** (3), 299 (1978).

³⁸X.-Q. Yan, X.-L. Zhang, S. Shi, Z.-B. Liu, and J.-G. Tian, Opt. Express **19** (6), 5559 (2011).

³⁹A. Zakery and S. R. Elliott, J. Non-Cryst. Solids **330** (1), 1 (2003).

⁴⁰J. M. Harbold, F. Ilday, F. W. Wise, J. S. Sanghera, V. Q. Nguyen, L. B. Shaw, and I. D. Aggarwal, Opt. Lett. **27** (2), 119 (2002).

⁴¹R. W. Boyd, *Nonlinear optics* (Academic press, 2003).

⁴²A. Sharon, D. Rosenblatt, and A. A. Friesem, Appl. Phys. Lett. **69** (27), 4154 (1996).

⁴³I. Karatzas and S. Shreve, *Brownian motion and stochastic calculus*, vol. 113 (Springer Science & Business Media, 2012).

⁴⁴D. Rosenblatt, A. Sharon, and A. A. Friesem, IEEE Journal of Quantum electronics **33** (11), 2038 (1997).

⁴⁵C. J. Chang-Hasnain and W. Yang, Advances in Optics and Photonics **4** (3), 379 (2012).

⁴⁶G. Levy-Yurista and A. A. Friesem, Appl. Phys. Lett. **77** (11), 1596 (2000).

⁴⁷J.-L. Adam and X. Zhang, *Chalcogenide glasses: preparation,*

- properties and applications* (Woodhead Publishing, 2014).
- ⁴⁸K. Y. Yang, D. Y. Oh, S. H. Lee, Q.-F. Yang, X. Yi, B. Shen, H. Wang, and K. Vahala, *Nature Photonics* p. 1 (2018).
- ⁴⁹J. S. Blakemore, *J. Appl. Phys.* **53** (10), R123 (1982).
- ⁵⁰M. Naftaly, J. Molloy, B. Magnusson, Y. Andreev, and G. Lanskii, *Optics express* **24** (3), 2590 (2016).